

Robotic Through-Wall Imaging

Saandeep Depatla*, Chitra R. Karanam*, and Yasamin Mostofi

Abstract—The overall goal of this paper is to present the new possibilities created at the intersection of robotic path planning and inverse scattering for through-wall imaging with everyday RF signals. More specifically, we are interested in the through-wall imaging of a completely unknown space using unmanned vehicles and with everyday RF transceivers. We first focus on robotic through-wall imaging based on only WiFi received signal power measurements (RSSI). In our second case, we then focus on robotic imaging based on only UWB signals, motivated by the new commercially-available chipsets that can provide a lightweight solution for small robotic platforms. The paper then shows that through proper path planning, sparse signal processing, and wave modeling, high-resolution through-wall imaging of a completely unknown space is possible with ubiquitous RF transceivers. We present several experimental results for robotic through-wall imaging of several different unknown spaces, comparing WiFi and UWB-based approaches. We then extensively discuss the impact of robotic path design on imaging, which provides general guidelines for robotic path planning in the context of through-wall imaging.

I. INTRODUCTION

Using electromagnetic waves for sensing has been of interest to the research community for many years. More recently, sensing with lower frequencies such as with radio waves, even with WiFi, has become of interest due to factors such as safety and availability of the transceivers. In particular, there has been a considerable interest in using Radio Frequency (RF) signals to sense and obtain information about the environment in various contexts, such as imaging, localization, tracking and occupancy estimation [1]–[10]. See-through imaging (also known as through-wall imaging) has in particular been of considerable interest to the research community. The ability to see through occluded objects can be beneficial to many applications such as search and rescue, surveillance and security, archaeological discovery, detection/classification of occluded objects, and medical applications. Despite great interest in this area, however, see-through imaging is still a considerably challenging problem, especially with everyday RF signals.

Recent progress in robotics, on the other hand, has created the possibility of unmanned autonomous vehicles helping us achieve tasks. Robotic networks can have a tremendous impact in many areas such as disaster relief, emergency response, environmental monitoring, surveillance, and security.

In this paper, we are interested in using unmanned vehicles for see-through imaging to enable imaging that is typically deemed not possible with static antennas. More specifically, we are interested in the scenario where two unmanned vehicles are tasked with imaging a completely unknown area, without any prior measurements, to which we refer as robotic see-through imaging. Fig. 3a shows a real example of the considered scenario. We first focus on **robotic through-wall imaging**

based on only WiFi RSSI (Received Signal Strength Indicator) signals. In other words, in our first case, WiFi received signal power is the only signal available for imaging. More specifically, both robots are equipped with WiFi cards and the receiving robot measures the received signal power of the transmitting robot. In our second case, we consider **robotic imaging based on only UWB signals.** While most UWB transceivers have been bulky and expensive, the new commercially-available chipset from DecaWave [11] (see Fig. 3d) provides a light-weight solution, with stable measurements for the power and time of arrival of the first path, which we shall utilize in our second case.

Literature Survey: A survey of the existing literature reveals a great body of work from various communities, e.g., electromagnetics, signal processing, and networking, on different aspects of RF sensing and through-wall imaging. In the electromagnetics community, for instance, there has been a considerable interest in solving the inverse scattering problem [12], [13]. More specifically, various full-wave solutions are obtained by using iterative techniques [14], contrast source inversion [15], and stochastic optimization [16]. Several linearizing approximations, such as Born and Rytov, are also proposed [2], [17], [18] to reduce the computational complexity in imaging. To reduce the number of required measurements, compressive sensing techniques have been utilized under these linear approximations [19]–[21]. However, there are very few experimental results reported with these approximations, especially at microwave frequencies or WiFi, due to the difficulty of the hardware setup and testing.

Assuming that phase can be measured, beam forming and time-reversal MUSIC are proposed to focus in a direction or image a target [1], [22], [23]. Radar systems have also been extensively used for remote sensing and target detection [24], [25]. Synthetic Aperture Radar (SAR) utilizes motion of the radar to synthesize a large antenna array to improve the resolution of remote sensing [26]. Using Ultra WideBand (UWB) signals can increase the resolution [3], but has traditionally required specialized and bulky hardware [27], making them not suitable for small robotic platforms.

In general, several existing work utilizes simulations for validation purposes due to the difficulty of the hardware setup and testing. Thus, the full benefits of the theoretical methods may not be realizable in real scenarios. Furthermore, for the case of through-wall imaging, the information of the first layer of occluders (such as the wall) is usually assumed via prior measurements [4], [28], [29]. Recently, a few methods propose to mitigate the effect of the walls [30]–[32]. However, these methods typically have experimental constraints, either on the locations along which the measurements are collected, or on the properties of the wall, and are furthermore focused on localizing the objects as opposed to detailed imaging. Also, in most setups, sensors are on one side of the wall and thus a reflection-based approach is typically utilized for through-

* Joint first authors. The authors are with the Department of Electrical and Computer Engineering, University of California, Santa Barbara, CA 93106, USA. {saandeep, ckaranam, ymostofi}@ece.ucsb.edu. This work is funded by NSF CCSS award # 1611254.

wall imaging. Finally, several existing work relies on the availability of the phase information or having a very large bandwidth. Even then, the problem of see-through imaging of completely unknown areas with everyday RF signals is still a considerably challenging problem, which is the main motivation for this paper.

In this paper, we show the possibilities and challenges created by using unmanned vehicles for through-wall imaging with ubiquitous RF signals. We do not assume any knowledge of the walls and as such, reconstruct the walls as well. Using unmanned vehicles can considerably reduce the burden of fixed antenna positioning as the vehicles can autonomously collect several RF measurements along their trajectories. More importantly, the fact that they have control over their trajectories has a great potential for improving see-through imaging through proper path planning. Finally, since two unmanned vehicles move outside of the area of interest, they can do tomographic imaging, i.e., one robot transmits a signal, which will interact with the area of interest as it goes through it. The receiving robot then measures the corresponding receptions (see Fig. 3a for an example). Using the transmission through the area, as opposed to reflections, is more suitable when no phase measurement is assumed, which is the case in this paper. In our past work, we have shown the first demonstration of imaging with WiFi in 2010 [33], and the first demonstration of through-wall imaging with WiFi in 2012 [7], followed by several other work [8], [9]. In this article, we build on our past work to present a comprehensive foundation for imaging through walls with unmanned vehicles. Additionally,

- We propose an UWB-based robotic imaging approach based on the first path power and time-of-arrival, and experimentally and extensively validate it utilizing new commercially-available UWB chipsets from DecaWave. We further extensively compare WiFi and UWB-based approaches.
- We show the impact of antenna directionality on the imaging quality. As we shall see, while utilizing a directional antenna improves the imaging quality, through-wall imaging with omni-directional antennas is also possible when utilizing the proposed robotic framework.
- We analyze the impact of large amount of robot localization errors on the imaging performance. The results indicate robustness to localization errors, even for values with a standard deviation as high as 10 cm per position.
- We present several see-through experimental results, involving objects with different material properties.

Overall, this article showcases the created possibilities for imaging with everyday RF signals when using unmanned vehicles.

The paper is organized as follows. In Section II, we mathematically formulate our problem, and discuss the wave modeling, signal processing, and path planning aspects of it. In Section III, we show experimental results for robotic through-wall imaging of several different unknown spaces. Section IV then explores the impact of different robotic paths on imaging, and discusses the underlying tradeoffs in terms of diversity and spatial resolution. We conclude in Section V.

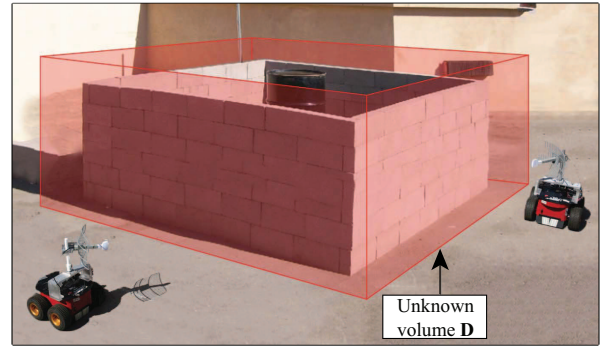


Fig. 1. The objective of the robots is to image the completely unknown workspace \mathbf{D} , shown with a superimposed red volume. Note that there are several objects which are completely occluded by the outer brick walls, requiring through-wall imaging. In this paper, we first consider robotic imaging based on only WiFi RSSI signals. This is then followed by robotic imaging based on only UWB signals.

II. A FOUNDATION FOR ROBOTIC THROUGH-WALL IMAGING

A. Problem Formulation

Consider a workspace \mathbf{D} that is completely unknown, i.e., it contains objects whose shapes, locations, or material property are completely unknown. Furthermore, several objects may be occluded by walls or other objects. Fig. 1 shows an example of our considered scenario. Two robots come to outside of the area of interest. One of the robots transmits Radio Frequency (RF) signals while the other robot measures the corresponding received signal. These scattered signals interact with the unknown area and thus implicitly contain information about the objects in \mathbf{D} . *Our objective is then to use robots to image the unknown workspace \mathbf{D} , by which we mean determining the location and geometry of all the objects in \mathbf{D} , without any a priori measurements.*

In this section, we start by summarizing the volume integral equations to model the received electric field in terms of the objects in \mathbf{D} and the positions of the Transmitter (TX) and Receiver (RX) robots. We then discuss linearizing approximations to formulate our problem as a linear inverse scattering problem, which we then solve to image \mathbf{D} using sparse signal processing and path planning. Consider the electric field in \mathbf{D} which is induced by the signal transmitted from the TX robot. The following volume integral equation then characterizes the received electric field at any position $\mathbf{r} \in \mathbb{R}^3$ [34]:

$$\mathbf{E}(\mathbf{r}) = \mathbf{E}_{\text{inc}}(\mathbf{r}) + \iiint_{\mathbf{D}} \vec{\mathbf{G}}(\mathbf{r}, \mathbf{r}') \bullet (O(\mathbf{r}')\mathbf{E}(\mathbf{r}')) dv', \quad (1)$$

where $\mathbf{E}(\mathbf{r})$ is the received electric field at \mathbf{r} , $\vec{\mathbf{G}}(\mathbf{r}, \mathbf{r}')$ is the free space tensor Greens function, $O(\mathbf{r}) = k^2(\mathbf{r}) - k_0^2$ denotes the material property of the object at position \mathbf{r} , $k_0^2 = \omega^2 \mu_0 \epsilon_0$ denotes the wavenumber of the free space, $k^2(\mathbf{r}) = \omega^2 \mu_0 \epsilon(\mathbf{r})$ denotes the wavenumber of the medium at \mathbf{r} , $\epsilon(\mathbf{r})$ denotes the electric permittivity at \mathbf{r} , ϵ_0 and μ_0 are the permittivity and permeability of the free space respectively, ω is the angular frequency, \bullet denotes the vector dot product, and $\mathbf{E}_{\text{inc}}(\mathbf{r})$ is the incident field at \mathbf{r} when there are no objects in \mathbf{D} . The first term of Eq. 1 then describes the field due to the presence of a source and the second term describes the field due to scattering from objects in \mathbf{D} . If the source is linearly polarized, then, by

neglecting the cross polarization terms in the scattered field, we can simplify Eq. 1 to the following scalar form [8]:

$$E(\mathbf{r}) = E_{\text{inc}}(\mathbf{r}) + \iiint_{\mathbf{D}} g(\mathbf{r}, \mathbf{r}') (O(\mathbf{r}') E(\mathbf{r}')) dv', \quad (2)$$

where $g(\mathbf{r}, \mathbf{r}')$ is the scalar Greens function.

Linearizing Approximations:

Equation 2 relates the received electric field $E(\mathbf{r})$ to the objects in \mathbf{D} . However, since the field $E(\mathbf{r}')$ inside the integral of Eq. 2 depends on $O(\mathbf{r}')$, Eq. 2 can be highly non-linear in \mathbf{D} due to multiple scattering [34]. As discussed in Section I, full-wave solutions can be obtained for Eq. 2 [14]–[16]. However, these methods have prohibitive computational complexity, especially for the sizes of the workspace \mathbf{D} considered in this paper. Therefore, we utilize approximations to linearize and then solve Eq. 2 by utilizing proper robotic path planning and sparse signal processing. These approximations only consider single scattering from objects in \mathbf{D} , neglecting multiple scattering [34]. Next we present two such approximations, which will work well for our robotic see-through imaging, as we shall see in the next sections.

1) *Line Of Sight (LOS) Approximation:*¹ At high frequencies², a wave predominantly propagates in a straight line, with negligible reflections or diffractions along its path [34]. Then a LOS-based approximation can model the field well and we can assume that the field at the receiver only depends on objects along the line joining the TX and the RX, which results in the following solution to Eq. 2 [34]:

$$E(\mathbf{r}) = \frac{c_0}{\sqrt{\alpha(\mathbf{r})}} e^{j\omega \int_{\mathbb{L}_{T \rightarrow R}} \alpha(\mathbf{r}') dr'}, \quad (3)$$

where $\alpha(\mathbf{r})$ is a complex number that represents the slowness of the medium at \mathbf{r} and is related to $k(\mathbf{r})$, $\int_{\mathbb{L}_{T \rightarrow R}}$ is a line integral along the line joining the positions of the TX and the RX, and c_0 is a constant that depends on the transmitted signal strength. In this paper, however, we assume WiFi frequencies such as 2.4 GHz, which is not high enough. Still, the LOS-based approximation can be informative for our robotic imaging problem, as we shall see in the next sections. The received power is then given by the following [8]:

$$P_r(\mathbf{r})(\text{dBm}) = P_{\text{inc}}(\mathbf{r})(\text{dBm}) - 10 \log_{10}(e^2) \omega \int_{\mathbb{L}_{T \rightarrow R}} \text{Imag}(\alpha(\mathbf{r}')) dr', \quad (4)$$

where $P_r(\mathbf{r})(\text{dBm})$ is the received power in dBm at \mathbf{r} , $P_{\text{inc}}(\mathbf{r})(\text{dBm})$ is the power incident in dBm at \mathbf{r} when there are no objects in \mathbf{D} , and $\text{Imag}(\cdot)$ denotes the imaginary part of the argument. $P_{\text{inc}}(\mathbf{r})(\text{dBm})$ can be estimated by robots making measurements in free space [8]. By discretizing the space and subsequently Eq. 4, we get the following linear equation:

$$\mathbf{P} \approx A_{\text{LOS}} \mathbf{O}_{\text{L}}, \quad (5)$$

where $\mathbf{P} = \frac{P_r(\text{dBm}) - P_{\text{inc}}(\text{dBm})}{10 \log_{10}(e^{-2})}$, A_{LOS} is a matrix of size $M \times N$ with its entry $A_{\text{LOS}_{i,j}} = 1$ if the j^{th} cell is along the line

joining the TX and RX of the i^{th} measurement, and $A_{\text{LOS}_{i,j}} = 0$ otherwise, M and N denote the number of measurements and size of the discretized unknown space respectively, $\mathbf{O}_{\text{L}} = [\alpha_1(\mathbf{r}_1) \alpha_1(\mathbf{r}_2) \cdots \alpha_1(\mathbf{r}_N)]^T$, $\mathbf{r}_1, \mathbf{r}_2 \cdots \mathbf{r}_N$ denote the positions of the cells in the workspace, and $\alpha_1(\cdot) = \text{Imag}(\alpha(\cdot))$.

2) *Rytov Approximation:* Although the LOS-based approximation accounts for single scattering from objects in \mathbf{D} , only those objects along the LOS are considered. In order to incorporate the effect of scattering from all the objects in \mathbf{D} in a linear model, we next consider the Rytov approximation [34]. Then, the solution to Eq. 2 is approximated by

$$E(\mathbf{r}) = E_{\text{inc}}(\mathbf{r}) e^{j\phi(\mathbf{r})}, \quad (6)$$

where

$$\phi(\mathbf{r}) = \frac{-j}{E_{\text{inc}}(\mathbf{r})} \iiint_{\mathbf{D}} g(\mathbf{r}, \mathbf{r}') O(\mathbf{r}') E_{\text{inc}}(\mathbf{r}') dv'. \quad (7)$$

We then have the following approximation for the received power for this case [8]:

$$\mathbf{P} \approx A_{\text{Ryt}} \mathbf{O}_{\text{R}}, \quad (8)$$

where $\mathbf{O}_{\text{R}} = \text{Real}(\mathbf{O})$ and $\text{Real}(\cdot)$ denotes the real part of the argument. Detailed analysis of the validity of these approximations can be found in [34].

B. Robotic Through-Wall Imaging

In this section, we first focus on robotic through-wall imaging based on only WiFi RSSI signals in Section II-B1, providing an overview of the formulation of [8]. In other words, in our first case, WiFi RSSI signals are the only signals available for imaging. More specifically, both robots are equipped with WiFi cards and the RX robot measures the received signal power from the transmissions of the TX robot. Considering this case is important as WiFi cards are readily available and the RSSI signal can be easily measured in the receiver.

In our second case in Section II-B2, we then consider robotic imaging based on UWB signals. This case is motivated by the emergence of small UWB chipsets that can be easily added to a small robotic platform, as discussed in Section I. We then extensively compare these two cases in our next section. We next briefly discuss these two cases in the context of the previous linear approximations.

1) *Robotic Through-Wall Imaging Using Only WiFi RSSI Signals:* In this case, Eq. 5 or 8 can be directly used. More formally, we will have [7], [8]:

$$\mathbf{P}_{\text{WiFi}} = \mathbf{A} \mathbf{X}, \quad (9)$$

where \mathbf{P}_{WiFi} is the accumulated vector of the received RSSI measurements as the robots move outside the area. Matrix \mathbf{A} is A_{LOS} for the LOS case and A_{Ryt} for the Rytov case respectively. Then, we solve for \mathbf{X} , which will be the estimated image. Although the estimated \mathbf{X} will be an estimate of \mathbf{O}_{L} for the LOS case and \mathbf{O}_{R} for the Rytov case, both are non-zero at locations where there are objects and zero otherwise allowing us to image the area.

¹This is also referred to as WKB approximation [34].

²In this paper, high frequency refers to the frequencies at which the size of the inhomogeneity of the objects is much larger than the wavelength.

2) *Robotic Through-Wall Imaging Using Only UWB Signals*: For the case of UWB transceivers, we utilize power of the first arrived path as well as its corresponding time-of-arrival (ToA). These two measurements are reliably provided by the new small UWB cards.³

The scattered power of the first path is typically affected by the objects near and along the line joining the transceivers. Thus, the LOS-based modeling of Section II-B can well approximate this case, as follows:

$$\mathbf{P}_{\text{UWB,FP}} \approx A_{\text{LOS}} \mathbf{X}_{\text{P}}, \quad (10)$$

where $\mathbf{P}_{\text{UWB,FP}}$ is the received power of the first path of the UWB signal, A_{LOS} is as defined in Section II-A, and \mathbf{X}_{P} is the image-related vector to solve for.

Next, we consider the ToA of the first path that reaches the receiver in each transmission. The time taken for a signal to travel a distance δ through a homogeneous material of permittivity ϵ is given by $\frac{\delta\sqrt{\epsilon'}}{c}$ [36], where c is the speed of light, and $\epsilon' = \text{Real}(\frac{\epsilon}{\epsilon_0})$. Let $t_1(\mathbf{p}_i, \mathbf{q}_i)$ and $t_0(\mathbf{p}_i, \mathbf{q}_i)$ denote the ToA of the first path and the ToA in free space respectively, where \mathbf{p}_i and \mathbf{q}_i denote the locations of the TX and RX respectively for the i^{th} measurement. Then, the difference between these times will be as follows:

$$t(\mathbf{p}_i, \mathbf{q}_i) = t_1(\mathbf{p}_i, \mathbf{q}_i) - t_0(\mathbf{p}_i, \mathbf{q}_i) = \int_{\mathbb{L}_{T \rightarrow R}} \frac{\sqrt{\epsilon'(\mathbf{r})} - 1}{c} d\mathbf{r}. \quad (11)$$

By discretizing Eq. 11, we get

$$t(\mathbf{p}_i, \mathbf{q}_i) = \sum_{j \in L_i} \frac{\Delta d}{c} (\sqrt{\epsilon'_j} - 1), \quad (12)$$

where L_i is the set of all the cells that lie on the line joining the TX and RX for the i^{th} measurement, $i \in \{1, 2, \dots, M\}$, M is the number of measurements, Δd is the cell size, $\epsilon'_j = \epsilon'(\mathbf{r}_j)$, and \mathbf{r}_j is the position of the j^{th} cell. The discretization is made small enough so that each cell can be assumed homogeneous, having the same permittivity throughout the cell. By stacking up all the measurements, we get the following linear equation for the ToA of the first path:

$$\mathbf{T}_{\text{UWB}} \approx A_{\text{LOS}} \mathbf{\Lambda}, \quad (13)$$

where $\mathbf{\Lambda}$ represents the relative times to be estimated, with the key feature that its corresponding value will be zero if there is no object at the corresponding position and non-zero otherwise, allowing us to form an image of the area from the estimate of $\mathbf{\Lambda}$.

Let $\hat{\mathbf{X}}_{\text{UWB,p}}$ and $\hat{\mathbf{\Lambda}}_{\text{UWB,t}}$ be the solutions of Eq. 10 and 13 respectively. Although $\hat{\mathbf{X}}_{\text{UWB,p}}$ and $\hat{\mathbf{\Lambda}}_{\text{UWB,t}}$ represent different physical properties of the objects in \mathbf{D} , both solutions are non-zero at locations where there is an object and zero otherwise. Thus, we can jointly use them to image the objects as follows:

$$\hat{\mathbf{X}}_{\text{UWB}} = f(\hat{\mathbf{X}}_{\text{UWB,p}}, \hat{\mathbf{\Lambda}}_{\text{UWB,t}}), \quad (14)$$

³In a general UWB transceiver, one can measure the power-delay profile (ToA and power of a number of paths). However, we find the power-delay profile measurement not as stable in the small UWB chipset [11], Decawave EVK1000, as also reported by other users [35]. Thus, in this paper we only rely on using the power and ToA of the first path, which can be reliably measured in Decawave EVK1000 cards.

where f is a function that efficiently combines the information in $\hat{\mathbf{X}}_{\text{UWB,p}}$ and $\hat{\mathbf{\Lambda}}_{\text{UWB,t}}$, and $\hat{\mathbf{X}}_{\text{UWB}}$ is the overall estimate of the unknown space. More details on f is given in Section III.

C. Sparse Signal Processing and Image Reconstruction

In the previous section, we posed a number of linear equations that related the measurements to the properties of the objects in the unknown space. Let N and M denote the size of the discretized space and the total number of measurements respectively. Typically, due to the size of workspace of interest to this paper and the difficulty of collecting a prohibitive number of measurements, we will have $M \ll N$. This leads to an under-determined system of equations in 9, 10 and 13. Therefore, to get a meaningful solution to these equations, we need to take advantage of the underlying sparsity of the area of interest. More specifically, many real physical spaces are sparse in the space domain or in their spatial variations [7], allowing us to utilize tools from sparse signal processing [37], which we briefly summarize next. Consider the following general linear equation:

$$\mathbf{Y} = B\mathbf{Z}, \quad (15)$$

where $\mathbf{Z} \in \mathbb{R}^N$ is a general unknown signal, $\mathbf{Y} \in \mathbb{R}^M$ is the measurement vector and B is an $M \times N$ observation matrix. Suppose \mathbf{Z} is sparse in some domain, i.e.,

$$\mathbf{Z} = \Theta \mathbf{z}, \quad (16)$$

where Θ is an invertible matrix and \mathbf{z} is S -sparse, i.e., $\text{card}(\text{supp}(\mathbf{z})) = S$ where $\text{card}(\cdot)$ denotes the cardinality of the argument and $\text{supp}(\cdot)$ denotes the set of indices of the non-zero elements of the argument. If $N \geq 2S$, then the solution to Eq. 15, under specific conditions [37], is given by the following optimization problem:

$$\text{minimize } \|\mathbf{z}\|_0, \quad \text{subject to } \mathbf{Y} = K\mathbf{z}, \quad (17)$$

where $K = B\Theta$. This means we only require $2S$ measurements to recover \mathbf{Z} . However, the above problem is non-convex and combinatorial in nature. The following is then the convex relaxation of the above problem:

$$\text{minimize } \|\mathbf{z}\|_1, \quad \text{subject to } \mathbf{Y} = K\mathbf{z}. \quad (18)$$

In the compressive sensing literature [37]–[39], it has been well established that solving Eq. 18 can solve the original problem of Eq. 17 if the matrix K satisfies the Restricted Isometry Condition (RIC) [39]. In the context of our considered robotic through-wall imaging, we have shown that certain motion patterns result in a matrix K that satisfy the RIC condition in [7]. Several of the considered areas are also sparse in their spatial variations. Thus, minimizing the spatial variation can also provide an alternative to the ℓ_1 relaxation, with a lower computational complexity [7]. In this paper, we thus focus on total variation minimization. More specifically, let $R = [R_{i,j}]$ denote an $m \times n$ matrix that represents the unknown space. Then we solve the following Total Variation (TV) minimization problem:

$$\text{minimize } \text{TV}(R), \quad \text{subject to } \mathbf{Y} = K\mathbf{z}, \quad (19)$$

where $\text{TV}(R) = \sum_{i,j} \|\mathbf{D}_{i,j}(R)\|$, denotes the spatial variations of the unknown space, where $\mathbf{D}_{i,j}(R) = [D_{h,i,j} \ D_{v,i,j}]$, $D_{h,i,j} = \begin{cases} R_{i+1,j} - R_{i,j} & \text{if } 1 \leq i < m, \\ R_{i,j} - R_{1,j} & \text{if } i = m, \end{cases}$, $D_{v,i,j} =$

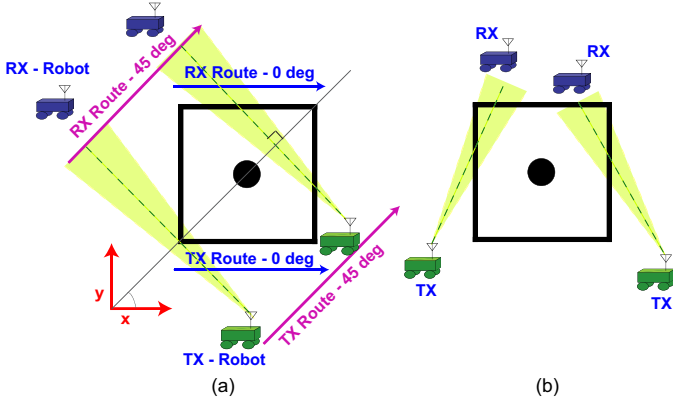


Fig. 2. An illustration of (a) semi-parallel robotic routes and (b) random routes, as defined in [8]. The left figure shows sample semi-parallel routes at 0 and 45 degrees. Random routes refer to routes that do not have a specific pattern.

$$\begin{cases} R_{i,j+1} - R_{i,j} & \text{if } 1 \leq j < n, \\ R_{i,j} - R_{i,1} & \text{if } j = n. \end{cases}$$
 , and $D_{h,i,j}$ and $D_{v,i,j}$ denote the spatial variations in the horizontal and vertical directions respectively. The linear equation of 19 can then represent any of the equations 9, 10, or 13. We make use of MATLAB-based solver TVAL3 [40] to solve the above optimization problem in the next sections.

The solution obtained by solving this optimization problem corresponds to a grayscale image reconstruction of the unknown space. Since we are only interested in imaging the locations and shapes of the objects (as opposed to the material properties), we further make use of the two-level Otsu thresholding method [41] in the next section. By utilizing the Otsu method, the cells in the unknown space are optimally classified as empty or occupied, thereby providing a binary object image of the unknown area.

D. Robotic Path Planning

The main strengths of using unmanned vehicles for through-wall imaging are two-folds: 1) the TX and RX antennas can be easily and autonomously positioned in many locations along a trajectory of the robots, a task that is prohibitive and challenging without unmanned vehicles, and 2) through proper path planning, the TX and RX locations can be properly optimized to be those most informative for imaging. More specifically, the paths that the robots take directly affect matrix K in Eq. 19 and thus the imaging quality considerably. We next summarize two possible motion patterns of [8], [9]. In the first pattern, which is motivated by computed tomography, the robots take routes that we refer to as “semi-parallel”. More specifically, consider the workspace of Fig. 2a and the line that passes through the origin at angle θ . We say that the robots are taking a semi-parallel route at angle θ if the TX and RX robots move such that the line connecting the two is orthogonal to the line that passes through the origin at the angle θ . Fig. 2a shows two such sample routes at 0° and 45° .⁴ Then, the non-zero elements in each row of matrix K correspond to the pixels in the unknown space that are visited by the line joining the TX and RX. As we shall see in Section IV, semi-parallel routes can be very informative for robotic imaging. Thus, in the next

⁴Note that the robots do not have to necessarily move in parallel. Thus, we refer to this pattern as semi-parallel.

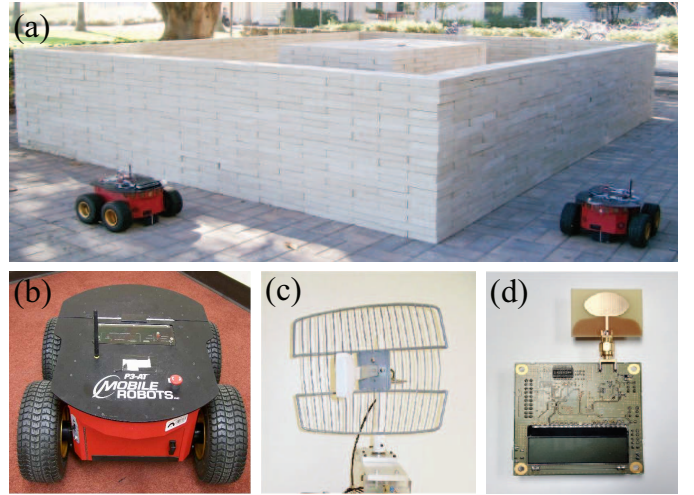


Fig. 3. Experiment setup and the corresponding hardware components – (a) two robots making measurements outside an unknown space in order to image the entire area including both occluded and non-occluded parts, (b) a pioneer 3-AT robot, (c) a directional parabolic grid antenna (GD24-15 2.4GHz) that will be used in some of the experiments when imaging with WiFi, and (d) a DecaWave EVK1000 transceiver with an omni-directional antenna, which will be used when imaging with UWB signals.

section, we first show several experimental results with such routes. We then extensively summarize the interplay between path planning and robotic imaging in Section IV. In addition to semi-parallel routes, we also consider the case where the TX and RX robots do not take a specific pattern and take wireless measurements anywhere possible. This case is referred to as “random” motion pattern. We emphasize that the robots do not necessarily have to take a randomized route but “random” here means that no specific pattern is taken. Fig. 2b shows an example of the random case. We then utilize the random pattern in Section IV, in conjunction with semi-parallel routes, to discuss the underlying tradeoffs in path planning and robotic imaging.

III. EXPERIMENTAL RESULTS

In section II, we extensively discussed through-wall imaging based on either only WiFi RSSI signals or only UWB signals (first path power and ToA). In this section, we show the performance of this framework with several real structures. We start by summarizing our experimental setup.

A. Summary of Experimental Setup

Our setup consists of two Pioneer 3-AT mobile robots [42], shown in Fig. 3b, which move outside of the unknown area of interest and collect wireless measurements. Fig. 3a shows one example where the robots are making measurements in a real environment to image a completely unknown area. The robots are programmed to autonomously move along any set of given routes and collect wireless measurements. When moving outside of the area of interest, the two robots do not coordinate their movement. Rather, each one traverses its given trajectory and estimates its own position and the position of the other robot based on the assumed constant speed. Our current localization error is less than 2.5 cm for every 1 m of straight line movement. For the lengths of routes considered in this paper, it is shown in [8] that localization errors and the associated antenna alignment errors (when

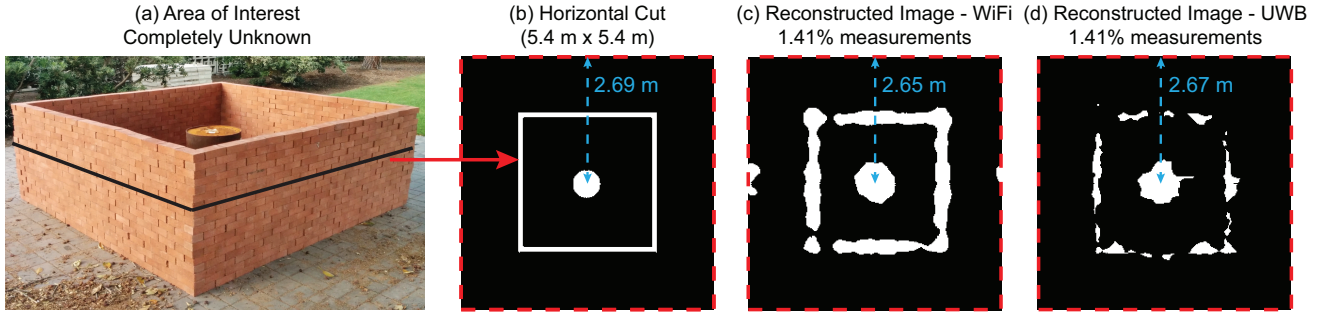


Fig. 4. (a) The area of interest that is completely unknown, (b) a 2D horizontal cut of it, which has the dimension $5.4 \text{ m} \times 5.4 \text{ m}$, with the red dashed lines indicating the boundary of the unknown area to be imaged, (c) reconstructed image with 1.41% WiFi RSSI measurements using LOS-based approximation, and (d) reconstructed image with 1.41% UWB transmissions.

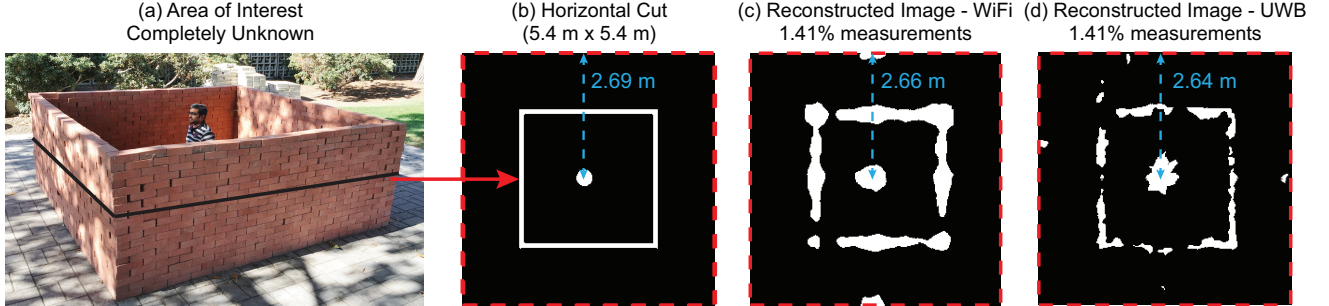


Fig. 5. (a) The area of interest that is completely unknown, (b) a 2D horizontal cut of it, which has the dimension $5.4 \text{ m} \times 5.4 \text{ m}$, with the red dashed lines indicating the boundary of the unknown area to be imaged, (c) reconstructed image with 1.41% WiFi RSSI measurements using LOS-based approximation, and (d) reconstructed image with 1.41% UWB transmissions.

directional antennas are used) have a negligible impact on the reconstruction quality of the image.

Imaging with Only WiFi RSSI Signals:

In this case, we use the experimental setup described in [8]. We next briefly summarize the setup here. The TX robot is equipped with a WBR-1310 wireless router, which acts as a WiFi signal source. The RX robot is equipped with an on-board IEEE 802.11g wireless network card (Atheros ar5006x), that can measure WiFi RSSI signals. As the robots move, the TX robot continuously transmits WiFi signals at +15 dBm, which are then measured by the WiFi card on the RX robot.

In some of the experiments with WiFi, we use directional antennas to limit scattering from objects that are not on the direct LOS. In this case, we use a GD24-15 2.4 GHz parabolic grid antenna from Laird Technologies [43] for wireless transmissions, which is shown in Fig. 3c. This model has a 15 dBi gain with 21° horizontal and 17° vertical beamwidth.

Imaging with Only UWB Signals:

For through-wall imaging with UWB signals, we mount a DecaWave EVK1000 transceiver chip [11] that is equipped with omni-directional antennas on each robot. The transceiver, shown in Fig. 3d, supports transmissions in six of the UWB channels outlined in the IEEE 802.15.4-2011 standard [44]. We use UWB transmissions at 3.99 GHz center frequency with a bandwidth of 900 MHz. This setup provides us with the power and ToA of the first path reaching the receiver, which we shall use for imaging.

Next, we present the performance of the through-wall imaging approach using this setup. We present WiFi-based imaging results for two new areas, along with two WiFi results considered in our previous work (albeit with some

improvement using Otsu's method) [7]–[9]. In Section III-C, we then show imaging results with only UWB signals. We further compare the performance of imaging based on WiFi RSSI and imaging based on UWB signals. In Section III-D, we present imaging of more complex areas. Finally, in Section III-E, we show the impact of antenna directionality on imaging based on WiFi RSSI signals by comparing the results of imaging with omni-directional and directional antennas. We note that, in all the results of this paper, we only consider imaging of an unknown area in 2D, i.e., we only image a horizontal cut of the unknown area. We, however, emphasize that the methodology of this paper can be generalized to 3D imaging as well.

B. Experimental Imaging Results with WiFi RSSI Signals

Fig. 4a shows the area of interest that is completely unknown, while Fig. 4b shows a horizontal cut of it. The unknown area to be imaged is marked with a red dashed-line boundary in 2D. We refer to this area as the *occluded cylinder*. The cylinder is metallic and the outer wall is made of concrete blocks. Note that the outer wall is also unknown and needs to be imaged. The size of the unknown area is $5.4 \text{ m} \times 5.4 \text{ m}$ with each pixel being $2 \text{ cm} \times 2 \text{ cm}$. Thus, the total number of unknowns amounts to 72,900. Two robots move outside of this area taking 4 semi-parallel routes that are explained in Section II-D, along 0, 90, 45, and 135 degrees. We use LOS-based approximation of Eq. 5 in this section. Furthermore, the robots use the directional antennas of Fig. 3c for all WiFi-based results of this section. We show results with WiFi RSSI and omni-directional antennas in Section III-E.

Fig. 4c shows the reconstruction with only 1.41% WiFi RSSI measurements (a cruder result for imaging this area with

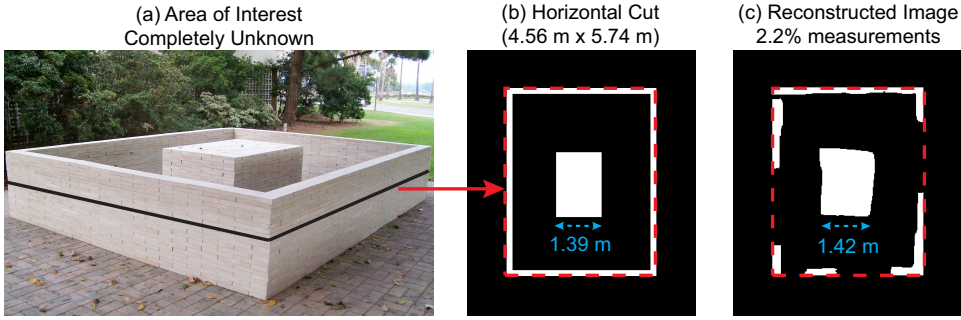


Fig. 6. (a) The area of interest that is completely unknown, (b) a 2D horizontal cut of it, which has the dimension $4.56 \text{ m} \times 5.74 \text{ m}$, with the red dashed lines indicating the boundary of the unknown area to be imaged, and (c) reconstructed image with 2.2% WiFi RSSI measurements using Rytov approximation.

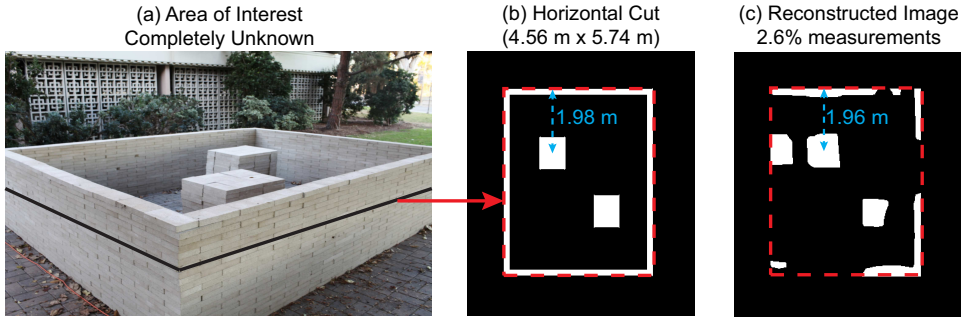


Fig. 7. (a) The area of interest that is completely unknown, (b) a 2D horizontal cut of it, which has the dimension $4.56 \text{ m} \times 5.74 \text{ m}$, with the red dashed lines indicating the boundary of the unknown area to be imaged, and (c) reconstructed image with 2.6% WiFi RSSI measurements using Rytov approximation.

WiFi was shown in [8]). The percentage measurement refers to the ratio of the total number of wireless measurements to the total number of unknowns (number of pixels of the unknown discretized space, e.g., 72,900 for Fig. 4) when expressed as a percentage. Two-level Otsu's thresholding method is utilized in order to obtain a binary reconstruction of the unknown area. Even with such a very small percentage of measurements, it can be seen that the locations and shapes of the objects are imaged well. For instance, the center of the cylinder is imaged at the distance of 2.65 m from top (see Fig. 4c), which is very close to the true distance of 2.69 m.

We next consider imaging another completely unknown area where the cylinder in Fig. 4 is replaced by a human. Fig. 5a shows the new considered scenario, with the human inside, while Fig. 5b shows a horizontal cut of it. We refer to this area as the *occluded human*. We use robotic routes identical to that of the occluded cylinder to collect wireless measurements, which results in 1.41% measurements. Fig. 5c shows the reconstructed image which is thresholded as described before. Similarly, we see that the objects are imaged with a good accuracy (compare 2.66 m imaged distance in Fig. 5c with 2.69 m true distance of Fig. 5b). It is noteworthy that the reduction in the size of the occluded object (when going from the cylinder to human) is well reflected in the reconstructed images. Overall, it can be seen that the robotic framework can image (image-through) highly-attenuating objects like concrete walls, metallic objects, and humans, with a high quality.

C. Experimental Imaging Results with UWB Signals

Next, we show the imaging results for the occluded cylinder and occluded human with UWB signals. As can be seen from

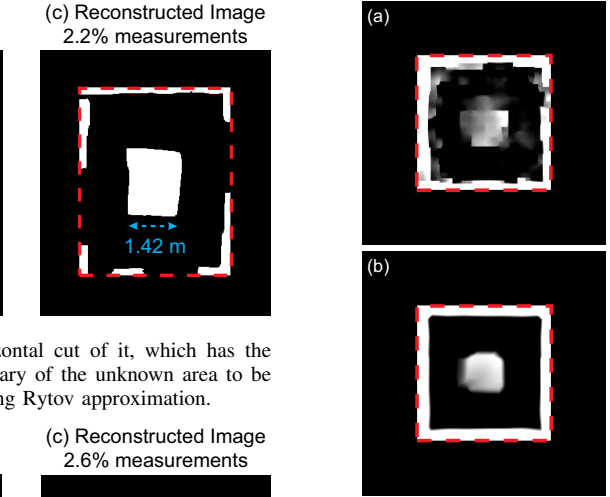


Fig. 8. Comparison of imaging with omnidirectional and directional antennas for the case of WiFi RSSI measurements and the unknown area of Fig. 4a. Rytov-based reconstructed image with 1.41% WiFi RSSI measurements using (a) omnidirectional and (b) directional antennas. While we expect to lose some imaging quality with omnidirectional antennas, we can still see fair amount of details. This is due to the fact that we can have a more optimized positioning of the TX and RX antennas with robots.

Eq. 14, our UWB imaging is based on both the ToA ($\hat{\Lambda}_{\text{UWB},i}$) and power of the first path ($\hat{\mathbf{X}}_{\text{UWB},p}$). These images are thresholded using the two-level Otsu's thresholding method. As for combining the two resulting images, i.e., choice of f of Eq. 14, we use the following approach. We consider a location in the final estimated image empty if the corresponding location in the thresholded $\hat{\Lambda}_{\text{UWB},i}$ or $\hat{\mathbf{X}}_{\text{UWB},p}$ is empty. Otherwise, we average the corresponding estimated intensity values to indicate the intensity of the object at that location followed by Otsu thresholding.

Fig. 4d and 5d show the reconstructed images for the cases of the occluded cylinder and occluded human respectively. The routes and the number of transmissions are the same as for the case of WiFi RSSI of Section III-B. As can be seen, the imaging quality is considerably high for both scenarios. As compared to the WiFi RSSI imaging results of Section III-B, the imaging results are comparable. This is due to the fact that we used directional antennas for the WiFi case of Section III-B, which limits the scattering from objects out of the LOS path, making the results comparable to the case of imaging with the first path/ToA of UWB signals. However, as the antennas get more directional, their size increases and it becomes difficult to use them with small mobile platforms. Thus, the UWB card of Fig. 3d, which is used in the experiments of this section, can be a promising choice for very small robotic platforms due to its small size ($7 \text{ cm} \times 11 \text{ cm}$).⁵ We note that while the total number of transmissions are the same for the WiFi results of Section

⁵Note that we do not utilize the full capabilities of UWB signals here, such as multiple frequencies and delay spread, as explained in the earlier sections.

III-B and the UWB results of this section, the case of UWB also utilizes the ToA information, which doubles the number of linear equations to be used (Eq. 10 and 13).

D. Imaging of More Complex Areas

We next discuss experimental results with more complex structures that have larger areas and multiple occluded objects. The robots use WiFi RSSI measurements in this section and the reconstructed images are obtained by using the Rytov approximation of Eq. 8 for the received signal. Furthermore, the reconstructions are thresholded as described for the WiFi imaging results of Section III-B. A comprehensive comparison of Rytov and LOS approximations, for WiFi-based imaging, is given in [8].

Fig. 6a shows the unknown area of interest, which has the size of $4.56 \text{ m} \times 5.74 \text{ m}$, while Fig. 6b shows a horizontal cut of it. As can be seen, the occluded middle area has a larger dimension, making the imaging more challenging. Both the outer wall and the inner rectangle of this structure are made of concrete bricks. The unknown area to be imaged is marked with a red dashed-line in 2D. Two robots take semi-parallel routes along 0, 90, 80, and -10 degrees. Fig. 6c shows the reconstructed image with 2.2% measurements. It can be seen that the reconstruction quality is very good. For instance, the width of the inner block is imaged at 1.42 m with the original size being 1.39 m.

Next, Fig. 7a shows the unknown area of interest, which has the size of $4.56 \text{ m} \times 5.74 \text{ m}$ with two objects inside, while Fig. 7b shows a horizontal cut of it. This whole area is made of concrete bricks. The unknown area to be imaged is marked with a red dashed-line in 2D. A robotic imaging of this area with WiFi is provided in [8]. Here, we summarize that result, but with an addition of Otsu's method, which improves the imaging quality considerably.

Two robots take semi-parallel routes along 0, 90, 80, 10, and -10 degrees. Fig. 7c then shows the imaging result based on only 2.6% measurements. Since this area is more complex, we expect the imaging quality to drop as compared to the previous results. However, the details of the inner blocks and outer wall are still imaged well, as can be seen, and a sample dimension of 1.98 m is imaged at 1.96 m. As compared to the result of [8] (Fig. 10), it can be seen that several of the faint false images are not present anymore by using Otsu's method.

E. Impact of Antenna Directionality

When showing the results with WiFi RSSI measurements in Section III-B, the robots used the directional antenna of Fig. 3c. Using directional antennas, when only having WiFi RSSI measurements, will help limit the scattering off of the objects that are not directly on the LOS path between the TX and RX. In this part, we show the imaging result if the robots use an omni-directional antenna instead, while imaging with WiFi RSSI signals.

More specifically, the robots use a dipole antenna at 2.4 GHz, which comes with the robots, instead of the directional antenna of Fig. 3c. Fig. 8 compares the imaging result of omni-directional and directional cases for the unknown area of Fig. 4a, based on the same robotic routes and number of wireless

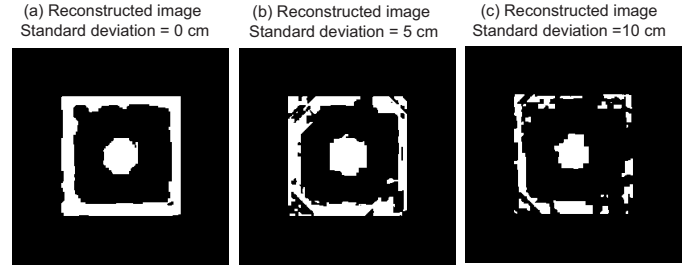


Fig. 9. The effect of a large amount of localization errors on robotic imaging. It can be seen that even with a position error with a standard deviation of 10 cm per position, the area can still be imaged with a reasonable quality.

transmissions of Fig. 4. Rytov approximation is utilized in these results and the area to be imaged is marked with a dashed red line. As expected, imaging with WiFi RSSI signals and with omni-directional antennas is more challenging. However, by utilizing semi-parallel robotic routes, the area can still be imaged, as can be seen. In other words, by utilizing robots for imaging, we have created the possibility of optimizing the positioning of the antennas, and subsequently extracting decent images from only WiFi RSSI signals and omni-directional antennas. In the next section, we extensively discuss the impact of robotic paths on imaging.

F. Impact of Robot Localization Errors

In imaging with unmanned vehicles, two robots move outside of the unknown area to collect wireless measurements, as discussed earlier. Each robot estimates its own position and the position of the other robot, when the wireless measurements are collected, based on the given constant speed. However, in harsh environments, there may be positioning errors, for instance, due to non-uniform robot speeds as a result of uneven ground conditions. Therefore in this section, we evaluate the impact of large amount of robot localization errors on the reconstruction quality.

In order to analyze the effect of localization errors, we next manually add large errors to the measurement locations. We note that the locations in the experimental measurements are already subject to small errors. But for the purpose of the analysis of this section, we assume that the localization errors in our experiments were negligible and manually add errors to the location stamps. We then use these highly-noisy measurement locations in the reconstructions. More specifically, we add a zero-mean Gaussian noise with a standard deviation of σ , to both the X and Y coordinates of the positions estimated by each robot. We then use these noisy measurement locations in the reconstructions.

Fig. 9 shows sample reconstructions with different amount of localization noise ($\sigma = 5$ and $\sigma = 10$), for the case of WiFi-based imaging of the unknown area of Fig. 4a, where the length and width of the wall are 2.98 m, thickness of the wall is 0.1 m, and the diameter of the occluded cylinder is 0.58 m. For comparison, we note that the errors encountered in our experiments are typically much smaller. For instance, in the experiments of Section III, the ground vehicles experience a localization error with an average standard deviation of 3.6 cm along the route and 1.45 cm along the direction perpendicular to the route. In this section, we then add an error with a

standard deviation as high as 10 cm to each location in both X and Y directions, which is much larger than the typical errors encountered in real experiments. It can be seen that while the imaging quality degraded for the case of $\sigma = 10$, as compared to $\sigma = 0$, we can still obtain an informative image despite the large amount of localization error. Furthermore, it is observed that a good reconstruction can still be obtained up to a standard deviation of $\sigma = 25$ cm, which is much larger than the typical errors in actual experiments. Similar observations have been made for other areas, thus establishing the robust nature of the framework to robot localization errors.

IV. ROBOTIC PATH PLANNING FOR IMAGING [9]

In the previous sections, we extensively discussed two approaches, WiFi-based and UWB-based, for robotic through-wall imaging and thoroughly validated them by experiments. We utilized two robots that moved in semi-parallel routes, as described in Section II, to image several real structures in our experiments. However, there are other possible routes that the robots can take, as established in [9]. Thus, for the sake of completion, in this section we then summarize the impact of the choice of the robotic routes on the imaging quality, building on [9] and highlighting the key insights.

We mainly focus on two broad motion patterns, “semi-parallel” and “random”, which were introduced in Section II-D and Fig 2. As we shall see, properly-designed semi-parallel routes can be considerably informative for imaging. However, the robots may not be able to always traverse such routes due to environmental/time constraints. Then, random motion patterns can be used and can even have a better performance than the semi-parallel ones under certain conditions, as we discuss in this section. We note that throughout this section, we use simulations for comparing different route designs. Specifically, for a given workspace and the routes for robots, we generate wireless measurements by using the LOS-based forward approximation. Still, the gained insights will be helpful when designing robotic routes in the experiments. We also note that the nature of this section is analytical in the sense that we explore the routes that could be most informative for imaging, with an emphasis on understanding the underlying tradeoffs.

A. Diversity of the Measurements

As defined in [9], let the spatial variations (jumps) of a 2D image along angle θ denote the variations of the line integral of the area, along lines orthogonal to the line at angle θ (e.g., see Fig. 2a). When the robots move on a semi-parallel route at angle θ , the measurements then naturally have the potential of capturing the spatial variations (jumps) of the unknown space along the direction θ if the robots transmit/receive at a high-enough spatial resolution along that route. For instance, Fig. 10 shows the 2D cut of the occluded cylinder scenario and the corresponding real measurements collected along a semi-parallel route at 0° , by using directional antennas and sampling at 2 cm intervals with WiFi signals. As can be seen, the measurements clearly reflect the spatial jumps of the unknown space along the 0° direction. Even without the use of directional antennas, we expect that the variations in

the power measurements along a semi-parallel route to be correlated with the spatial changes of the material property along that route. Thus, a semi-parallel route has the potential to capture the spatial changes of the area of interest along a particular route. However, a semi-parallel route at angle θ has a limited perspective of the unknown space, which is only along the direction θ , i.e., the robots can view the unknown space as a projection along only one direction. On the other hand, when the robots move in a random pattern, i.e., when they collect measurements from a few TX/RX position pairs in the workspace, they can potentially get multiple perspectives of the unknown space. However, in this case, the spatial jumps (variations) of the unknown space may not be clearly identified. In summary, the number of semi-parallel routes, their choice and the sampling resolution along each route can considerably affect the overall imaging performance.

Thus, we can ask the following question: “given a fixed number of wireless measurements that the robots can make, over what kind of routes should they be distributed?” We motivate the discussion by an example. Consider the occluded cylinder shown in Fig. 4a. Given an extremely small percentage of measurements of 0.77%, Fig. 11a shows the reconstructed image when the robots collect the measurements at random TX/RX position pairs in the workspace. On the other hand, Fig. 11b shows the corresponding reconstruction, when all the measurements are collected along the 0° robotic route. It can be seen that the semi-parallel case performs worse in this example. More specifically, it can be seen from Fig. 11b that the semi-parallel route along 0° clearly identifies the jumps in the unknown space, but only along the 0° direction. On the other hand, although the case of random does not clearly identify the boundaries, it results in a better overall reconstruction in this case.

Next, we increase the number of measurements to 4.6% in the bottom row of Fig. 11. In this case, the measurements of semi-parallel routes are distributed along 4 routes of 0, 90, 45 and 135 degrees, while the measurements of the random pattern are collected at randomly-distributed TX/RX position pairs outside of the unknown area. It can be seen from the reconstructions that the semi-parallel routes outperform in this case. This is because four semi-parallel routes can now measure the jumps along a few informative angles, providing both spatial resolution along each route and an overall diversity of views.

In summary, we see that semi-parallel routes can be considerably informative by capturing the spatial changes. However, it is important that they are diverse enough in terms of capturing the area from different perspectives. Therefore, given a number of wireless measurements, we need to identify the optimum number of angles over which they should be distributed. Distributing the measurements over a large number of angles results in more diversity at the cost of less spatial resolution along each route, presenting interesting tradeoffs. Furthermore, we need to identify which semi-parallel routes (what angles) are the most informative. In the next section, we start by discussing the choice of optimal angles for semi-parallel routes, followed by the optimum number of semi-parallel routes.

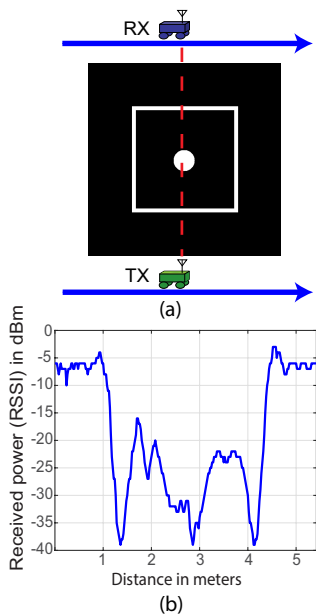


Fig. 10. (a) Occluded cylinder scenario of Fig. 4a with robots making measurements along 0° route and (b) the corresponding real WiFi RSSI measurements.

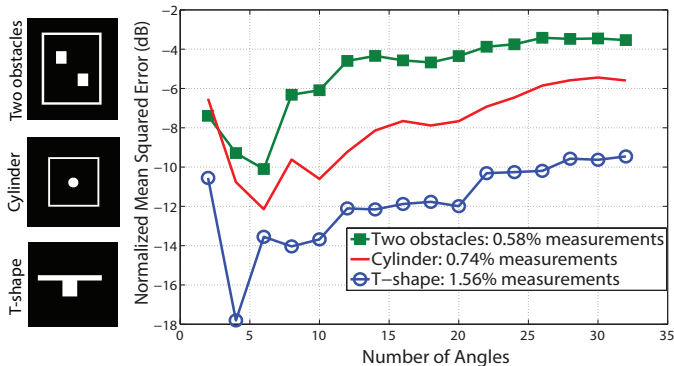


Fig. 13. Normalized Mean Square Error (NMSE) of imaging quality for the scenarios shown on the left, as a function of number of angles.

B. Optimal Choice of Angles for Semi-parallel Routes

As discussed in the previous section, a semi-parallel route along a given direction θ can capture the spatial variations of the unknown space along angle θ . Hence, when considering the choice of the angles, moving along the directions that contain the most spatial variations (jumps) in the unknown space would be more optimal.

As an example, consider the occluded cylinder shown in Fig. 4a, whose 2D cut is shown in Fig. 12a as well. This structure contains jumps mainly along 0° and 90° . Fig. 12b shows the reconstruction when measurements are collected along 30, 60, 120, and 150 degrees, and not along the main jump angles. It can be seen that the information about the walls is completely missing in the reconstruction. Next, we make measurements along the 90° angle instead of 120° , while retaining the other angles. Fig. 12c shows the reconstruction for this case. It can be seen that jumps along the 90° direction are now identified. Finally, we replace two of the angles with 0° and 90° , which are the main jump directions for this structure. As can be seen in Fig. 12d, the reconstruction is almost exact. This toy

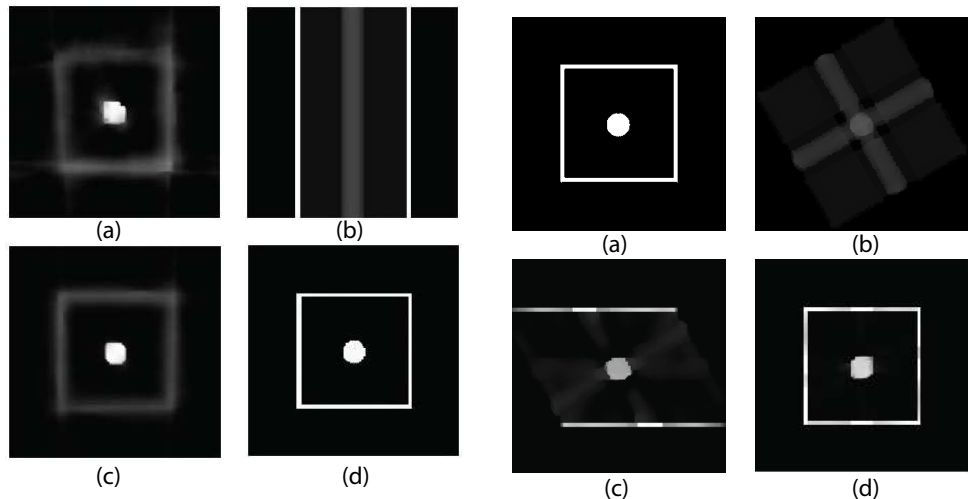


Fig. 11. Comparison of semi-parallel and random routes in imaging the occluded cylinder of Fig. 4a. Top row shows the imaging obtained with 0.77% measurements for (a) case of random routes and (b) case of semi-parallel routes along one angle. Bottom row shows imaging obtained with 4.6% measurements for (c) case of random routes and (d) case of semi-parallel routes along 4 routes.

Fig. 12. Comparison of imaging with different semi-parallel route angles for the occluded cylinder. (a) the true image, (b) imaging with no routes along the jump angles, (c) imaging with one route along one jump angle and (d) imaging with two routes along two jump angles. It can be seen that making measurements along jump angles gives a better reconstruction.

example confirms that moving along the angles with the most spatial jumps can be considerably informative for imaging. For a more formal information-theoretic proof of this for a simple structure, we refer the readers to our previous work [9]. We note that during their operation, the robots do not know the jump angles as the area is completely unknown to them. Thus, the insight from the aforementioned analysis can be utilized in two manners. First, it could be used in sequential imaging where the robots adapt their routes online based on the current reconstructed image. Second, several spaces have underlying patterns, for instance in terms of orthogonality of walls, which can be used to design the initial routes by the robots.

C. Optimal Number of Angles for Semi-parallel Routes

Consider the case where the robots can make a given number of measurements. We next consider the choice of the number of angles along which the robots should distribute their measurements. Intuitively, if they collect these measurements over a large number of angles, they have more diversity in sampling the space from different perspectives while the sampling resolution along each angle will be less, as discussed earlier. In this part, we discuss this while considering the optimum choice of angles.

Fig. 13 shows the imaging performance in terms of the Normalized Mean Square Error (NMSE), as a function of the number of angles, for three different structures shown on the left. For each structure, there is a given number of allowed measurements, as indicated in the caption. For each number of angles, first the angles corresponding to the directions of jumps are chosen. Then the remaining angles are chosen to have a uniform angle distribution. Furthermore, the total allowed measurements are distributed evenly among the given angles. It can be seen that for each structure, there is an optimum number of angles at which the imaging error is minimum, and this optimum strikes a balance between spatial resolution and

diversity for the structure. For instance, this optimum is 4 for the T-shape, while it is 6 for the other cases. In general, we can see that as the structure gets more complex, more randomness (diversity of views) may be needed through distributing the measurements among a larger number of angles [9].

V. CONCLUSIONS

The goal of this paper was to provide a comprehensive foundation for the possibilities at the intersection of robotics and inverse scattering for through-wall imaging. More specifically, we considered high-resolution through-wall imaging of completely unknown spaces using unmanned vehicles. In our first case, we focused on through-wall imaging based on WiFi RSSI signals, while in our second case we considered imaging based on first path power and time-of-arrival of UWB signals. The paper presented a framework for robotic through-wall imaging based on proper path planning, sparse signal processing, and linearized wave modeling, and confirmed it with several experimental results that involved imaging completely-unknown spaces with a variety of materials. The UWB and WiFi-based approaches are then extensively compared. Furthermore, the impact of antenna directionality was demonstrated. Overall, the paper can serve as a comprehensive reference for the possibilities created by utilizing unmanned vehicles for through-wall imaging.

REFERENCES

- [1] A.J. Devaney. Super-resolution processing of multi-static data using time reversal and music. 2000.
- [2] F. Soldovieri and R. Solimene. Through-wall imaging via a linear inverse scattering algorithm. *IEEE Geoscience and Remote Sensing Letters*, 4(4):513–517, 2007.
- [3] H. Wang, R.M. Narayanan, and O.Z. Zhou. Through-wall imaging of moving targets using UWB random noise radar. *IEEE Antennas and Wireless Propagation Letters*, 8:802–805, 2009.
- [4] F. Ahmad and M.G. Amin. Through-the-wall radar imaging experiments. In *2007 IEEE Workshop on Signal Processing Applications for Public Security and Forensics*, 2007.
- [5] S. Depatla, A. Muralidharan, and Y. Mostofi. Occupancy estimation using only wifi power measurements. *IEEE J. Selected Areas in Communications*, 33(7):1381–1393, 2015.
- [6] A. Ghaffarkhah A. Gonzales-Ruiz and Y. Mostofi. An Integrated Framework for Obstacle Mapping with See-Through Capabilities using Laser and Wireless Channel Measurements. *IEEE Sensors Journal*, 14(1):25–38, January 2014.
- [7] Y. Mostofi. Cooperative Wireless-Based Obstacle/Object Mapping and See-Through Capabilities in Robotic Networks. *IEEE Transactions on Mobile Computing*, DOI: 10.1109/TMC.2012.32, January 2012.
- [8] S. Depatla, L. Buckland, and Y. Mostofi. X-ray vision with only wifi power measurements using rytov wave models. *IEEE Trans. on Vehicular Technology*, 64(4):1376–1387, 2015.
- [9] A. Gonzalez-Ruiz and Y. Mostofi. Cooperative robotic structure mapping using wireless measurements a comparison of random and coordinated sampling patterns. *IEEE Sensors Journal*, 13(7):2571–2580, 2013.
- [10] C.R. Karanam and Y. Mostofi. 3D through-wall imaging with unmanned aerial vehicles using WiFi. In *Proceedings of the 16th ACM/IEEE International Conference on Information Processing in Sensor Networks*, pages 131–142. ACM, 2017.
- [11] DecaWave. <http://www.decawave.com/>.
- [12] D. Colton and A. Kirsch. A simple method for solving inverse scattering problems in the resonance region. *Inverse problems*, 12(4):383, 1996.
- [13] Y. Wang and W.C. Chew. An iterative solution of the two-dimensional electromagnetic inverse scattering problem. *International J. Imaging Systems and Technology*, 1(1):100–108, 1989.
- [14] W.C. Chew and Y. Wang. Reconstruction of two-dimensional permittivity distribution using the distorted born iterative method. *IEEE Trans. on Medical Imaging*, 9(2):218–225, 1990.
- [15] P. Van Den Berg, A. Van Broekhoven, and A. Abubakar. Extended contrast source inversion. *Inverse problems*, 15(5):1325, 1999.
- [16] M. Pastorino. Stochastic optimization methods applied to microwave imaging: A review. *IEEE Trans. on Antennas and Propagation*, 55(3):538–548, 2007.
- [17] A.J. Devaney. Inversion formula for inverse scattering within the born approximation. *Optics Letters*, 7(3):111–112, 1982.
- [18] G. Oliveri, L. Poli, P. Rocca, and A. Massa. Bayesian compressive optical imaging within the rytov approximation. *Optics Letters*, 37(10):1760–1762, 2012.
- [19] Andrea Massa, Paolo Rocca, and Giacomo Oliveri. Compressive sensing in electromagnetics—a review. *IEEE Antennas and Propagation Magazine*, 57(1):224–238, 2015.
- [20] Lorenzo Poli, Giacomo Oliveri, and Andrea Massa. Microwave imaging within the first-order born approximation by means of the contrast-field bayesian compressive sensing. *IEEE Transactions on Antennas and Propagation*, 60(6):2865–2879, 2012.
- [21] Qiong Huang, Lele Qu, Bingheng Wu, and Guangyou Fang. Uwb through-wall imaging based on compressive sensing. *IEEE Transactions on Geoscience and Remote Sensing*, 48(3):1408–1415, 2010.
- [22] M.J. Burfeindt, J.D. Shea, B.D. Van Veen, and S.C. Hagness. Beamforming-enhanced inverse scattering for microwave breast imaging. *IEEE Trans. on Antennas and Propagation*, 62(10), 2014.
- [23] P. Kosmas and C.M. Rappaport. Time reversal with the FDTD method for microwave breast cancer detection. *IEEE Trans. on Microwave Theory and Techniques*, 53(7):2317–2323, 2005.
- [24] J. Marcum. A statistical theory of target detection by pulsed radar. *IRE Trans. on Information Theory*, 6(2):59–267, 1960.
- [25] Y. Huang, P.V. Brennan, D.W. Patrick, I. Weller, P. Roberts, and K. Hughes. Fmcw based mimo imaging radar for maritime navigation. *Progress In Electromagnetics Research*, 115:327–342, 2011.
- [26] J.C. Curlander and R.N. McDonough. *Synthetic aperture radar*. John Wiley & Sons New York, NY, USA, 1991.
- [27] F. Sabath, D.V. Giri, F. Rachidi, and A. Kaelin. *Ultra-Wideband, Short-Pulse Electromagnetics 7*. Springer, 2007.
- [28] R. Chandra, A. Gaikwad, D. Singh, and M.J. Nigam. An approach to remove the clutter and detect the target for ultra-wideband through-wall imaging. *J. Geophysics and Engineering*, 5(4):412, 2008.
- [29] F. Ahmad, M.G. Amin, and S.A. Kassam. Synthetic aperture beamformer for imaging through a dielectric wall. *IEEE Trans. on Aerospace and Electronic Systems*, 41(1):271–283, 2005.
- [30] F. Ahmad, J. Qian, and M.G. Amin. Wall clutter mitigation using discrete prolate spheroidal sequences for sparse reconstruction of indoor stationary scenes. *IEEE Transactions on Geoscience and Remote Sensing*, 53(3):1549–1557, 2015.
- [31] Y.S. Yoon and M.G. Amin. Spatial filtering for wall-clutter mitigation in through-the-wall radar imaging. *IEEE Transactions on Geoscience and Remote Sensing*, 47(9):3192–3208, 2009.
- [32] F.H.C. Tivive, A. Bouzerdoum, and M.G. Amin. A subspace projection approach for wall clutter mitigation in through-the-wall radar imaging. *IEEE Transactions on Geoscience and Remote Sensing*, 53(4):2108–2122, 2015.
- [33] Y. Mostofi and A. Gonzalez-Ruiz. Compressive Cooperative Obstacle Mapping in Mobile Networks. pages 947–953, San Jose, CA, Oct. 2010.
- [34] W.C. Chew. *Waves and fields in inhomogeneous media*, volume 522. IEEE press New York, 1995.
- [35] Forum. https://groups.google.com/forum/#!forum/decawave_group.
- [36] M.G. Amin. *Through-the-wall radar imaging*. CRC press, 2016.
- [37] E. Candès, J. Romberg, and T. Tao. Robust uncertainty principles: Exact signal reconstruction from highly incomplete frequency information. *IEEE Trans. on information theory*, 52(2):489–509, 2006.
- [38] D.L. Donoho. Compressed sensing. *IEEE Trans. on Information Theory*, 52(4):1289–1306, 2006.
- [39] D. Needell and R. Vershynin. Uniform uncertainty principle and signal recovery via regularized orthogonal matching pursuit. *Foundations of computational mathematics*, 9(3):317–334, 2009.
- [40] C. Li, W. Yin, and Y. Zhang. Users guide for TVAL3: Tv minimization by augmented lagrangian and alternating direction algorithms. *CAAM report*, 20:46–47, 2009.
- [41] N. Otsu. A threshold selection method from gray-level histograms. *Automatica*, 11(285-296):23–27, 1975.
- [42] MobileRobots Inc. <http://www.mobilerobots.com>.
- [43] Laird Technologies. <http://www.lairdtech.com/Products/Antennas-and-Reception-Solutions/>.
- [44] *IEEE Standard for Local and metropolitan area networks—Part 15.4: Low-Rate Wireless Personal Area Networks (LR-WPANs)*, 802.15.4-2011, 2011.